Solid State Sciences 158 (2024) 107755

Contents lists available at ScienceDirect

Solid State Sciences

journal homepage: www.elsevier.com/locate/ssscie

In situ synthesis of metal-organic frameworks on sulfonated cellulose nanofibrils

Kailong Zhang [a], William Hutcherson [b], Neal D. Evans [c], Thomas Elder [d], Charles M. Garner [b], Mi Li [a,*]

[a] Center for Renewable Carbon, School of Natural Resources, The University of Tennessee, Knoxville, TN, 37996, USA
[b] Department of Chemistry, University of Memphis, Memphis, TN, 38152, USA
[c] UT Institute for Advanced Materials & Manufacturing, The University of Tennessee, Knoxville, TN, 37996, USA
[d] USDA-Forest Service, Southern Research Station, Auburn, AL, 36849, USA

ARTICLE INFO

Keywords:
Sulfonation
Cellulose template
Cellulose nanofibrils
Metal-organic frameworks
Adsorbent

ABSTRACT

The intrinsic fragility and inferior processibility of metal-organic frameworks (MOFs) particles often restrict their functional application despite their high surface area and porous structure. We investigated the feasibility of sulfonated cellulose nanofibrils (SCNF) as a biopolymer template to hybridize MOFs. SCNF was synthesized through periodate oxidation followed by bisulfite sulfonation. The sulfonate groups increased electronegativity and enhanced the dispersibility of the cellulose fibers. More importantly, the negatively charged sulfonates could serve as anchors for metal ions to initiate the *in situ* growth of MOFs along the surface of cellulose fibers. We have achieved the synthesis of three types of SCNF/MOF hybrids, namely, SCNF/ZIF-8, SCNF/ZIF-67, and SCNF/HKUST-1. These hybrids can be formed as free-standing aerogels, exhibiting remarkably high surface areas and flexibility for applications. The assessment of the adsorptive efficiency of the SCNF/ZIF-8 hybrid indicates that the hybrid material exhibited a notably higher adsorption capacity for methylene blue versus the SCNF control. DFT calculation provides further insights into the underlying adsorption mechanisms, revealing that the sulfonates on the SCNF and the nitrogen atoms in the ZIF-8 ligands primarily contributed to the affinity for methylene blue. SCNF offers a versatile and robust biopolymer substrate for templating a wide array of MOFs with promising applications as adsorbents and beyond.

1. Introduction

Metal-organic frameworks (MOFs), synthesized through the coordination of metal ions with multifunctional organic ligands, have gained increasing attention as novel porous materials owing to their ultra-high surface areas, high void volumes, low densities, and high thermal and chemical stabilities [1,2]. The tunable pore structure and adjustable functionality make MOFs highly suitable for many applications such as adsorbents, catalysis, sensing, conductors, and gas storage [3–67]. Innovations in functionality enhancement, controlled synthesis methods, and precise characterization have further broadened the application horizon of these multifaceted materials[8,9]. Nevertheless, the traditional solvothermal synthesis of MOFs often yields fine powders or small particles. Their intrinsic brittleness, aqueous insolubility, and lack of thermoplastic properties pose challenges to their processability and large-scale production and application [10].

Integrating MOFs with polymers is a feasible approach to enhance their processability, facilitating the formation of 2D or 3D materials with customized shapes and architectures. Among naturally derived polymers, cellulose nanofibrils (CNF) stand out as a promising option due to their abundance and sustainability. CNF is sourced from plant-based cellulose and mechanically refined into fibrils, featuring diameters less than 100 nm and lengths spanning several micrometers. The 2,2,6,6-tetramethylpiperidinyloxy (TEMPO)-mediated oxidation is a commonly used modification method that introduces carboxylate groups to the CNF surfaces. This modification increases CNF's hydrophilicity and aqueous dispersibility [11]. Meanwhile, the carboxylates on TEMPO-oxidized CNF serve as potential binding sites for metal ions, promoting *in situ* MOF nucleation and growth on the CNF surface [12]. The various forms of cellulosic products, such as fibers, membranes, papers, filters, aerogels, and hydrogels, make cellulose a suitable substrate to template MOFs by endowing them with macroscale architectures [13–15]. This

* Corresponding author.
E-mail address: mli47@utk.edu (M. Li).

https://doi.org/10.1016/j.solidstatesciences.2024.107755
Received 6 August 2024; Received in revised form 7 November 2024; Accepted 7 November 2024
Available online 9 November 2024

combination results in the development of multifunctional, easily processable, and synergistic hybrid materials. These CNF/MOF hybrids have applications across a variety of fields, such as water treatment, air purification, sensing, and drug delivery [12,16]. However, the strong tendency of TEMPO-oxidized CNF to agglomerate poses challenges to their use in practical applications. The abundant surface hydroxyl groups on the CNF can form hydrogen bonds with each other, resulting in self-aggregation within the fibers [17].

Sulfonated CNF (SCNF) is another modified form of cellulose in which the vicinal hydroxyls at C2 and C3 of the glucosyl units are converted into sulfonate groups ($–SO_3^-$) on the cellulose chains. SCNF is typically produced through a two-step process. First, cellulose is reacted with sodium periodate for oxidation, resulting in dialdehyde cellulose. This is followed by bisulfite sulfonation, during which the dialdehyde cellulose reacts with sodium bisulfite to introduce $–SO_3^-$ groups into the cellulose structure [18,19]. Integrating $–SO_3^-$ into cellulose increases the cellulose's charge density, reduces hydrogen bond formation, and minimizes fiber agglomeration during the drying process [20]. Prior research has indicated that $-SO_3^-$ possesses the ability to interact with metal ions through coordination [21,22]. More importantly, $-SO_3^-$ can form stable structures through coordination bonding effects, and these networks can exhibit functionality as well. Unlike the carboxyl group, which is limited to a planar configuration, the approximately spherical electron density surrounding the $–SO_3^-$ unit enables metal coordination in an extra dimension. This enhances the connectivity of the network and promotes the development of a stable structure [21,23]. Additionally, $–SO_3^-$ groups have also been found to enhance the transportation of cations, making SCNF a promising option as a green, ion-selective membrane for ionic transport [24]. This lays the foundation for SCNF as an alternative template for the *in situ* synthesis of MOFs. While TEMPO-oxidized CNF is widely studied as a substrate for MOF hybridization, to the best of our knowledge, the potential of SCNF as a templating substrate for MOF synthesis has rarely been examined. It is critical to explore alternative biopolymers that can hybridize and improve the performance of functional MOF. Our hypothesis is that SCNF, bearing negative $–SO_3^-$ on the fibrillar surface, can provide initial anchoring sites for metal ions deposition and *in situ* growth of linkers with better control of the dispersion of MOF along SCNF. We expect that SCNF will serve as a versatile and robust biopolymer substrate for templating different MOFs and exhibit an efficient adsorption capacity for pollutants.

In this study, we explored the feasibility of using SCNF as a templating scaffold for the *in situ* synthesis of different MOFs. To the best of our knowledge, this is the first attempt to produce SCNF/MOF hybrids. We prepared SCNF *via* a two-step process consisting of oxidation and bisulfite sulfonation of CNF. We investigated the capability of SCNF to support the *in situ* synthesis of ZIF-8 and examined the effect of the concentrations of the precursors. We then explored the effectiveness of SCNF as a template for the assembly of other MOFs including ZIF-67 and HKUST-1. Subsequently, the adsorptive capacity of the SCNF/ZIF-8 hybrid for methylene blue was assessed. Density Functional Theory (DFT) calculations were employed to offer insights into the mechanisms of the adsorption. Our study filled the gap of hybridization of alternative nanocellulose and MOF for advanced functional materials. We have demonstrated a new nanotechnology that could be applied for environmental remediation and beyond.

2. Materials and methods

2.1. Materials

CNF from softwood pulp with 3.1 *wt*% concentration in an aqueous slurry was purchased from the United States Department of Agriculture's Forest Products Laboratory (FPL, Madison, WI) and acquired through the Process Development Center in the University of Maine (Orono, ME, USA). The CNF is characterized by microscopy featuring a nominal fiber width of 50 nm and lengths extending to several hundred microns. Sodium periodate, sodium bisulfite, zinc nitrate hexahydrate, cobalt nitrate hexahydrate, copper nitrate, 1,3,5-benzenetricarboxylic acid (BTC), 2-methylimidazole, hydroxylamine hydrochloride, *tetra-n*-butylphosphonium bromide ([P4444]Br), and silver acetate (AgOAc) were purchased from Fisher Scientific. All the chemicals were analytical grade and used as received.

2.2. Preparation and characterization of SCNF

To prepare SCNF, 500 g of CNF slurry (1 *wt*%) was initially oxidized by adding 3.7 g of sodium periodate, and the mixture was stirred at 65 °C for 4 h in the absence of light. After the reaction, the oxidized CNF (OCNF) was immediately washed four times with DI water using centrifugation at 8,000 *g* for 10 min. Next, 1.2 g of sodium bisulfite was added to the OCNF for the sulfonation reaction, and the mixture was stirred at 40 °C for 3 h [19]. The SCNF was collected by redispersing and washing with DI water four times using centrifugation at 8,000 *g* for 10 min.

The degree of oxidation was determined by quantifying the aldehyde content according to published protocol using hydroxylamine hydrochloride [24,25,26]). Briefly, 0.1 g of freeze-dried OCNF was dispersed in 30 mL of 0.25 M hydroxylamine hydrochloride solution at pH 4, and the mixture was stirred for 2 h. Subsequently, the OCNF was removed by filtration, and the filtrate was titrated with 0.1 M NaOH until the pH returned to 4. The degree of oxidation was calculated based on the amount of NaOH consumed relative to the dry weight of the OCNF sample. The residual aldehyde content in SCNF was also measured using the same protocol. The measurements were conducted in triplicates.

The sulfonic acid content was determined by measuring the surface charge using conductometric titration [27]. A 0.5 *wt*% SCNF suspension was prepared in 50 mL DI water. The suspension was protonated by adjusting the pH to 1 with HCl, and the mixture was stirred at room temperature for 1 h. Subsequently, the SCNF was thoroughly washed with DI water using centrifugation to remove excess acid. Next, NaCl was added to the SCNF suspension to reach a final concentration of 1 mM. The conductivity was then titrated with 0.05 M NaOH until the lowest conductivity value was observed. The degree of sulfonation was calculated based on the amount of NaOH used in the titration. The measurement was conducted in triplicates.

For solution-state NMR analysis, the CNF and their derivatives were dissolved in *tetra-n*-butylphosphonium acetate ([P4444][OAc]) electrolyte per a previously published method [28]. Briefly, a methanol solution of [P4444]Br was subjected to a metathesis reaction with AgOAc to prepare [P4444][OAc]. The synthesized product was filtered through a 0.2 μm polypropylene membrane and subjected to rotary evaporation at 50 °C to remove residual water and methanol. The purified [P4444][OAc] was combined with DMSO-d_6 in a ratio of 1:4 (*wt/wt*) to prepare the stock electrolyte. The ^{1}H and ^{13}C NMR spectra of the electrolyte without sample were first acquired and provided in Fig. S1. For NMR analysis of cellulosic samples, approximately 25 mg of fiber samples were dissolved in 0.5 mL of the stock electrolyte at 65 °C. The ^{1}H, ^{13}C, and 2D HSQC NMR spectra were acquired using a Varian 400 MHz solution-state NMR spectrometer at 65 °C. A standard HSQC pulse sequence was used with the following acquisition parameters: spectra width 12 ppm in F2 (^{1}H) dimension with 1,024 data points (acquisition time 85.2 ms), 166 ppm in F1 (^{13}C) dimension with 256 increments (acquisition time 6.1 ms), a 1.0 s delay, a $^1J_{C–H}$ of 145 Hz, and 128 scans. The spectra were processed and analyzed using MestReNova software. The DMSO peak at $\delta_C/\delta_H = 39.5/2.49$ ppm was used as the internal reference for chemical shift calibration.

2.3. Preparation of SCNF/MOF hybrid

Three types of SCNF/MOF hybrids, namely, SCNF/ZIF-8, SCNF/ZIF-67, and SCNF/HKUST-1, were synthesized following previous protocols

[29,30]. First, three SCNF/ZIF-8 hybrids with varying ZIF-8 precursor concentrations were prepared. In each concentration, 7.5 mL of zinc nitrate hexahydrate in methanol (0.33 mmol, 1 mmol, or 3 mmol, respectively) was added to 15 mL of 0.2 % SCNF suspension in methanol and stirred at room temperature for 1 h. Then, 7.5 mL of 2-methylimidazole solution in methanol (2.67 mmol, 8 mmol, or 24 mmol, corresponding to the varying concentrations of zinc nitrate hexahydrate from low to high) was added dropwise to each of the above suspensions. Each resulting mixture was stirred at 25 °C for 2 h. The synthesized products were washed twice with methanol followed by once with DI water and centrifugation at 10,000 *g* for 10 min. Next, each product was dispersed in 30 mL of *t*-butanol and subjected to freeze drying. The final hybrids were marked as SCNF/ZIF-8 L, SCNF/ZIF-8 M, and SCNF/ZIF-8 H, representing low, medium, and high ZIF-8 precursor concentrations, respectively. Unless specified otherwise, SCNF/ZIF-8 in the following study refers to SCNF/ZIF-8 H.

To synthesize the SCNF/ZIF-67 hybrid, 7.5 mL of cobalt nitrate hexahydrate solution (3 mmol in methanol) was mixed with 15 mL SCNF suspension (0.2 % in methanol) and stirred for 1 h. A 7.5 mL of 2-methylimidazole solution (15 mmol in methanol) was then introduced, and the mixture was stirred at 25 °C for 24 h. For the synthesis of SCNF/HKUST-1 hybrid, 7.5 mL copper nitrate solution (3 mmol in methanol) was combined with 15 mL SCNF suspension (0.2 % in methanol) and stirred for 1 h. A 7.5 mL 1,3,5-benzenetricarboxylic acid solution (3 mmol in methanol) was then introduced, and the mixture was stirred at 25 °C for 2 h. Both the SCNF/ZIF-67 and SCNF/HKUST-1 were washed twice with methanol and once with DI water using centrifugation at 10,000 *g* for 10 min. Subsequently, the samples were freeze-dried following the same procedure employed for the SCNF/ZIF-8 hybrid.

2.4. Characterizations

The ζ-potential of CNF fiber samples and SCNF at0.5 *wt*% was measured using a Zetasizer Nano (ZS-90, Malvern Instruments, UK) in triplicate.

The micromorphology was characterized using a scanning electron microscope (SEM) equipped with an energy-dispersive X-ray spectrometer (EDS) system (Zeiss, EVO). The samples were sputter-coated with gold prior to observation.

The crystalline structure was analyzed using an X-ray diffractometer (XRD, PANalytical Empyrean) at 40 kV and 40 mA. Measurements were conducted at a 4° min^{-1} scanning rate with a 0.02° step size. The Miller indices were assigned according to the identified polymorphs [31]. The crystallinity index (CrI) of cellulose samples was determined using the following equation [32].

$$CrI\ (\%) = (I_{200} - I_{am}) / I_{200} \times 100$$

where I_{200} is the maximum XRD intensity at $2\theta = 22.6°$, and I_{am} is the intensity of the amorphous region at $2\theta = 18.9°$.

Attenuated total reflectance-Fourier transform infrared (ATR-FTIR) spectroscopy (PerkinElmer) was used to acquire the spectra through 16 scans, with a spectral range of 400–4,000 cm^{-1} and a 4 cm^{-1} resolution.

Thermogravimetric analyses (TGA) were carried out using a thermogravimetric analyzer (TGA Q50, TA Instruments-Waters). The samples were subjected to a temperature ramp from 30 °C to 800 °C at a rate of 10 °C/min. The mass ratio of ZIF-8 in the hybrid material was quantitatively assessed based on the TGA results [30].

Brunauer-Emmett-Teller (BET) specific surface area was assessed using N_2 adsorption-desorption isotherm measurements (Quantachrome Instruments). Samples (50–60 mg) were dried in tared tubes under vacuum (120 °C) overnight prior to reweighing. N_2 adsorption isotherms were measured at 77 K.

2.5. Adsorption of dye with SCNF/ZIF-8

The SCNF/ZIF-8 hybrid aerogel was fabricated using the same preparation protocol for SCNF/ZIF-8, with a 2 % concentration of SCNF to obtain a more structurally stable aerogel. After the synthesis, this SCNF/ZIF-8 hybrid was dispersed in water and subjected to freeze-drying to yield the free-standing aerogel. A control sample of pristine 2 % SCNF aerogel was also prepared.

To assess the adsorption capacities of the SCNF/ZIF-8 hybrid aerogel, 20 mg of aerogel was submerged in 20 mL of a methylene blue water solution (pH = 7) with concentrations of 5, 10, 20, 50, and 100 mg/L and shaken at 50 rpm. A UV–Vis spectrophotometer was used to determine the concentration of methylene blue at 665 nm. The adsorption capacity (Q_e, mg/g) of methylene blue was calculated using the following equation:

$$Q_e = \frac{(C_0 - C_e) \times \mathrm{V}}{m}$$

where C_0 (mg/L) represents the initial concentration of methylene blue, and C_e (mg/L) is the concentration of methylene blue at adsorption equilibrium. The mass of the SCNF/MOF adsorbent is given by m (g), and V (L) represents the dye solution's volume.

2.6. DFT calculation

DFT calculations were performed using Gaussian 16. To optimize computational efficiency, a representative cluster model comprising one zinc ion and three imidazolate ligands was employed to mimic the local reactive sites in ZIF-8 [33]. The structure of the SCNF was simplified to a glucose monomer with sulfonic acid groups as a representative SCNF model. The M06-2X functional was selected to conduct geometry optimization and frequency analysis. The computations were performed using the 6–31++G(d,p) basis set [34]. The adsorption energy, ΔE, quantified the interaction between SCNF/ZIF-8 clusters and methylene blue. It was calculated with a BSSE correction [35] as:

$$\Delta E = E_{complex} - (E_{adsorbent} + E_{mb})$$

where $E_{complex}$ represents the energy of the SCNF/methylene blue or ZIF-8/methylene blue complex, $E_{adsorbent}$ represents the energy of SCNF or ZIF-8 cluster, and E_{mb} represents the energy of methylene blue. The calculation results were visualized using VMD and Multiwfn software [36].

3. Results and discussion

3.1. Sulfonation and characterization

The sulfonation of CNF was achieved by using sodium periodate that selectively oxidized the C2 and C3 hydroxyl groups in the anhydroglucose repeating units of cellulose, forming 2,3-dialdehyde cellulose (OCNF). The aldehyde content in OCNF was determined to be 2.10 mmol/g (Table S1). The highly reactive aldehyde group in OCNF serves as an intermediate for the derivatization of cellulose [37]. The $–SO_3^-$ was introduced through sulfonating the aldehyde groups with sodium bisulfite (Fig. 1a) [19]. After sulfonation, the sulfonic acid content in SCNF was measured at 0.65 mmol/g, while the residual aldehyde content was found to be 1.30 mmol/g (Table S1). These results suggest that a portion (~30 %) of the aldehyde groups in OCNF were converted into sulfonic acid groups. The ζ-potential of the original CNF was measured to be 6.0 ± 0.9 mV. After sulfonation treatment, the introduction of $–SO_3^-$ decreased the ζ-potential of SCNF to −34.3 ± 3.1 mV. These negatively charged groups led to an electrostatic repulsion between the cellulose fibers, resulting in the formation of a clear and homogeneous gel mixture (Fig. 1a) where the SCNF was dispersed evenly throughout the liquid. SEM images demonstrated the micromorphology of the CNF

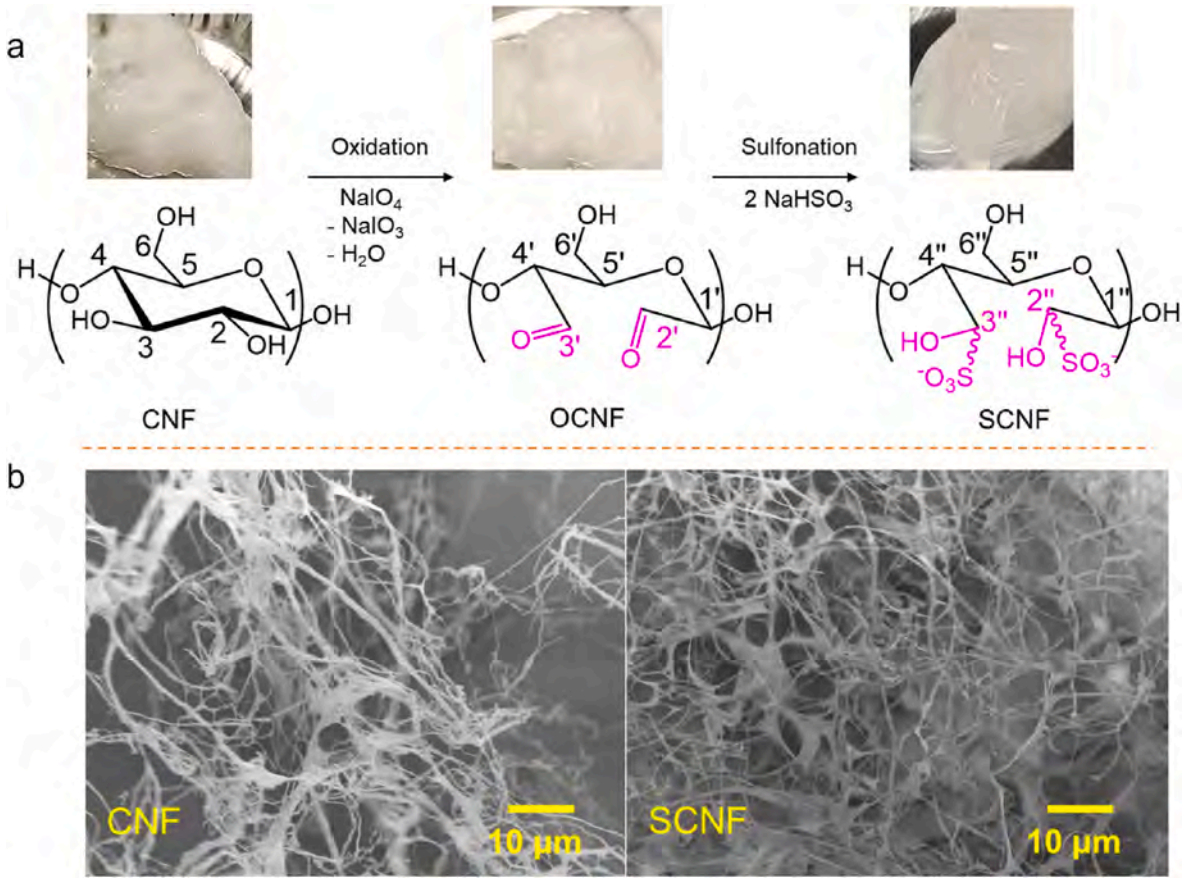

Fig. 1. Illustration of the oxidative-sulfonation reaction of CNF (a) and SEM images of CNF and SCNF (b).

and SCNF (Fig. 1b). After sulfonation, SCNF maintained the nanoscale features of the original CNF as a fibrillar shape with length of a few microns and diameters less than 1 μm. The fibrils of the SCNF were more uniformly distributed and exhibited less agglomeration than the original CNF. This could be attributed to the enhanced charge density on the nanofibrils that caused electrostatic repulsion between the nanofibrils.

The solution-state ^{13}C NMR spectra were characterized by dissolving the fibers in the [P4444][OAc] ionic liquid electrolyte [28]. As depicted in Fig. 2, the signals at 102.5, 78.5, 75.4, 74.5, 73.1, and 60.1 ppm were assigned to the C1, C4, C5, C3, C2, and C6 carbons of the glucopyranoside ring in CNF, respectively [27,28]. These signals were consistent with those observed in the HSQC spectra, as shown in Fig. S2. The characteristic ^{13}C peaks of CNF were identical across all the fiber samples. The oxidation of the C2 and C3 was expected to induce a downfield shift in the NMR signals of these carbons [27,38]. Accordingly, the signals observed at 97.7 and 92.2 ppm in the OCNF spectrum were

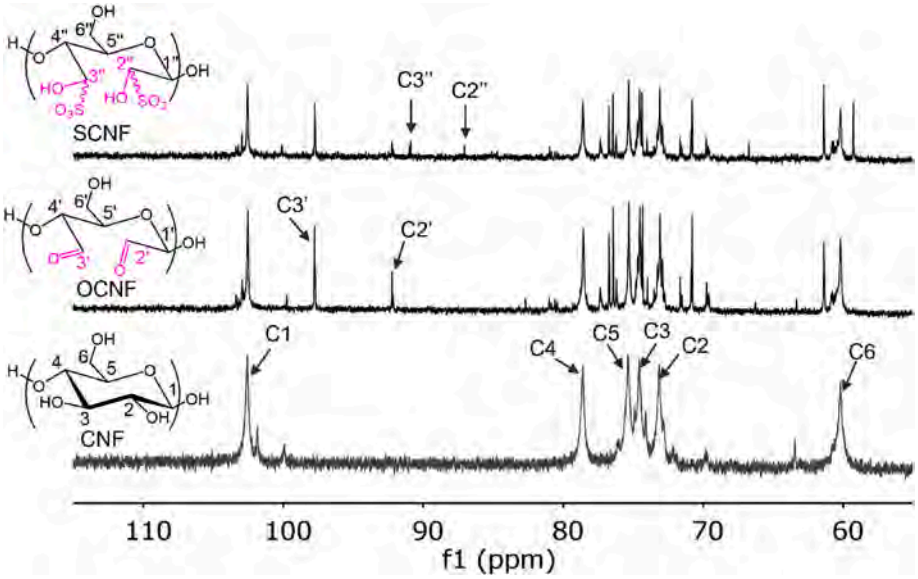

Fig. 2. Solution-state ^{13}C NMR spectra of CNF, OCNF, and SCNF obtained using [P4444][OAc]:DMSO-d_6 = 1:4 (*wt/wt*) at 65 °C.

tentatively attributed to the shifts of C2 and C3, respectively. In the SCNF spectrum, the signals at 90.8 and 80.7 ppm indicated a further shift of the C2 and C3 signals, which is attributed to the introduction of sulfonic acid groups at these positions. These new signals were also consistent with the HSQC spectra (Fig. S2). A new peak observed at 59.2 ppm in the SCNF spectrum was not assigned, which might be due to sulfonic acid groups' interactions with the ionic liquid electrolyte or impurity.

ATR-FTIR spectra (Fig. 3) were collected to characterize the chemical structure changes after oxidation and sulfonation. In the spectra of OCNF, a characteristic peak for the carbonyl group at 1,728 cm^{-1} was observed, indicating the formation of dialdehyde group following periodate oxidation [27]. Upon sulfonation, the intensity of the 1,728 cm^{-1} peak in the spectra of SCNF diminished, suggesting modifications to some dialdehyde groups due to sulfonation. Moreover, a prominent change was observed at 1,233 cm^{-1}, corresponding to the symmetric S–O stretching vibration [39]. Peaks at 1,058 cm^{-1} and 1,032 cm^{-1} are associated with C–C and C–O stretching vibrations, respectively. After oxidation and sulfonation, the intensity ratio of these peaks in OCNF and SCNF showed a decrease compared to the untreated CNF, indicating a potential disruption in the C2–C3 bond within the glucose ring [40]. These spectroscopic results corroborate the successful oxidation and sulfonation of CNF. The sulfonation modification of CNF was further examined using EDS as shown in Fig. S3a. The two spectra were scaled to the same level using the intensity of carbon (C) as the reference. Distinct peaks of C and oxygen (O) were identified in both CNF and SCNF. The peaks for carbon overlapped due to the scaled height used in the analysis. The sulfur (S) peak in the SCNF confirmed the presence of sulfur elements within the sample. Furthermore, the sodium (Na) peak observed in the SCNF spectrum was attributed to the sodium ions that bonded to $–SO_3^-$. The observed peaks for Aluminum (Al) and Silicon (Si) were attributed to the background signals originating from the substrate used for mounting the sample. These findings support and validate the sulfonation of CNF.

TGA was conducted to investigate the thermal stability of SCNF. Both CNF and SCNF exhibited three primary stages of weight loss during thermogravimetric analysis. The first stage, which occurred between 100 and 150 °C, was ascribed to the dehydration of cellulose (Fig. S3b). The second stage, occurred between 200 and 350 °C, corresponding to the decomposition of cellulose chains and the breaking of glycosidic bonds, resulting in the formation of low molecular weight compounds

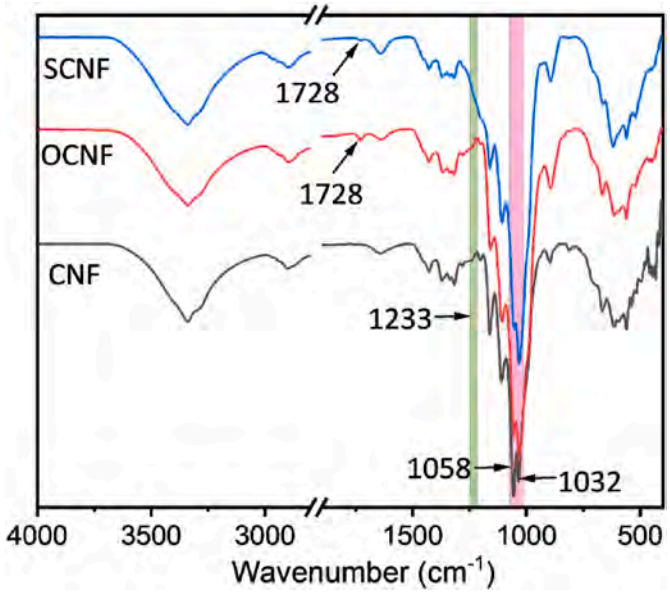

Fig. 3. FTIR spectra of CNF, OCNF, and SCNF.

such as levoglucosan [41]. The third stage occurred between 350 and 500 °C and involved the decomposition of the remaining carbonaceous residue [42]. The differential TGA (DTG) curve revealed that the maximum decomposition temperature of SCNF was 324 °C, which was lower than that of CNF at 344 °C. This implies that SCNF had a lower thermal stability, making it more susceptible to decomposition than CNF. Prior research has also highlighted a notable reduction in the thermal stability of cellulose following sulfonation [43]. The decreased stability might result from the oxidative and sulfonation treatments that open the six-atom ring structure, potentially reducing the stability of the cellulose skeleton and the crystalline structure [43,44]. XRD results indicate that the sulfonation treatment significantly compromised the cellulose crystallinity. The CrI of CNF decreased from 70.3 % to 40.2 % in SCNF as depicted in Fig. S3c. Cellulose crystallinity is primarily attributed to the parallel alignment of linear chains of glucose molecules. The hydrogen bonds formed between hydroxyl groups and oxygens in adjacent glucose monomers contribute to the stabilization of the crystalline regions [45]. In this study, the oxidation and sulfonation treatments altered the glucose ring structure of the cellulose. This alteration could disrupt the linear arrangement and rigidity of the individual cellulose chains and compromise their hydrogen bonding network, leading to a reduction in crystallinity [46].

3.2. Synthesis and characterization of SCNF/ZIF-8 hybrids

SCNF nanofibrils, with a high aspect ratio exceeding 100 and inherent flexibility, offer a suitable fibrillar scaffold for MOF particles. Their dimensions extend several micrometers in length and are less than 1 μm in diameter, making them well-suited to align with nano- or micro-scaled MOFs during synthesis. TEMPO-oxidized CNF, which is a widely-studied substrate for MOF templating, has its carboxylate groups acting as nucleation sites for MOFs [12]. These carboxylate groups enable the *in situ* growth of ZIF-8 on cellulose fibers, generating hybrid structures with dimensions that vary from several hundred nanometers to a few micrometers [30]. We contend that SCNF bearing negatively charged $–SO_3^-$ groups is analogous to the TEMPO-oxidized CNF bearing negatively charged carboxylate groups and may serve as the initiating sites for the positively charged metal ions followed by the coordination of organic ligands. Here, we have achieved the *in situ* synthesis of ZIF-8 on the flexible and fibrous SCNF, affording SCNF/ZIF-8 hybrids. As depicted in Fig. 4a, the SCNF/ZIF-8 hybrids showed a pearl necklace-like morphology. The hybrids featured dodecahedron-shaped ZIF-8 particles, around 400 nm in diameter, that were neatly and securely anchored to the SCNF fibers. The hybrid itself was measured at 1–2 μm in diameter, and no significant ZIF-8 self-agglomeration was observed. Further EDS mapping analysis revealed a consistent distribution of zinc elements across the SCNF's surface (Fig. 4a). The *in situ* synthesis entailed the integration of SCNF with Zn^{2+} and 2-methylimidazole precursors in a single reaction pot. Previous research has indicated a notable electrostatic attraction between $–SO_3^-$ and Zn^{2+} with a bonding energy of −5.24 eV [22]. The successful hybridization of SCNF with well-distributed ZIF-8 suggests that the $–SO_3^-$ on the SCNF was crucial in binding with the Zn^{2+} as nucleation sites. When imidazolate was introduced, the zinc ions coordinated with imidazolate linkers in a tetrahedral arrangement, resulting in a 3D porous crystalline structure on the SCNF surface [47]. The role of SCNF as a biopolymer template for the formation and growth of MOF is closely comparable to the TEMPO-oxidized CNF.

Powder XRD was used to identify the phases within the SCNF/ZIF-8 hybrid. Due to the organic fiber nature of SCNF, the diffraction intensity of SCNF is considerably lower compared with that of ZIF-8 because the latter has a well-coordinated crystalline structure. As a result, only the crystallinity of ZIF-8 was discernible from the spectra (Fig. 4b). The XRD peaks at 2θ values of 7.4, 10.5, 12.8, and 18.1° were assigned to the characteristic planes (110), (200), (211), and (222) of ZIF-8 crystals, respectively, confirming the presence of ZIF-8 crystals on the SCNF. ATR-FTIR spectra were also obtained to examine the ZIF-8 and SCNF

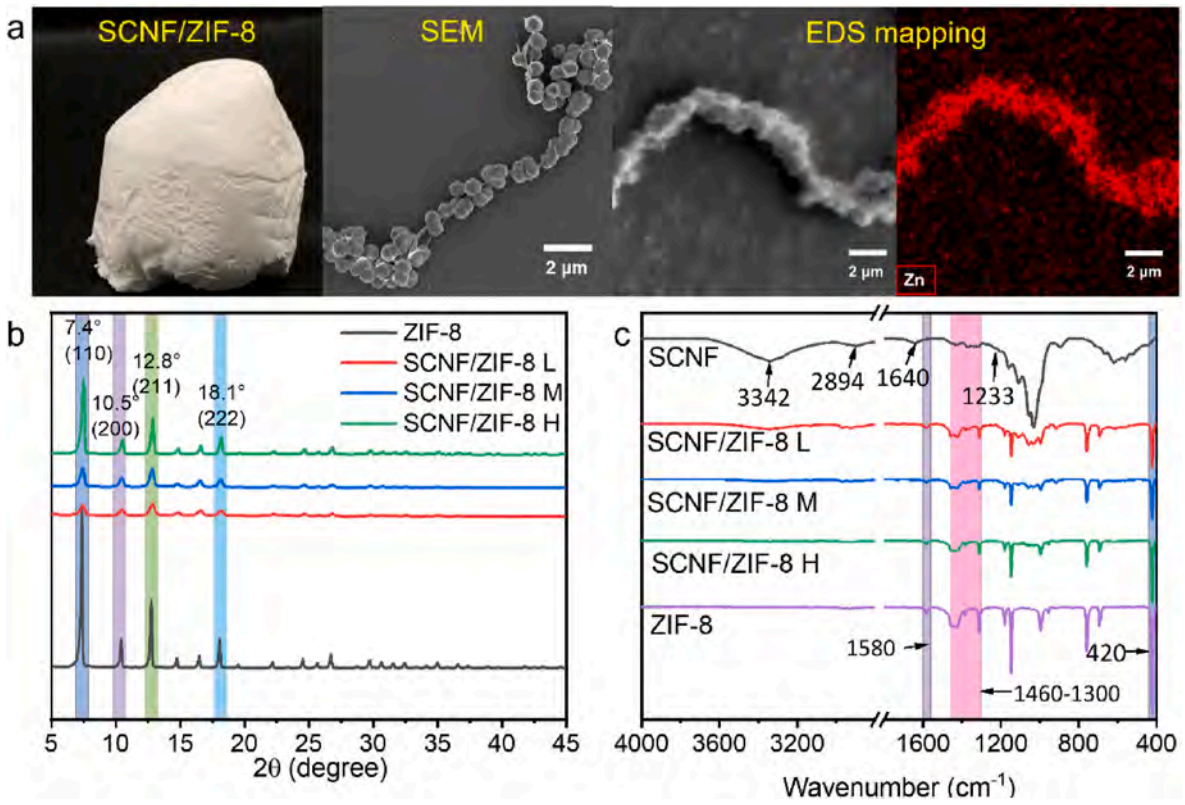

Fig. 4. Characterization of SCNF/ZIF-8: visual appearance, SEM images, and EDS mappings (a), XRD patterns (b), and FTIR spectra (c).

hybrids (Fig. 4c). The peaks of SCNF at 3,342, 2,894, 1,640, and 1,233 cm^{-1} were attributed to the stretching vibrations of –OH, C–H, C=O, and S–O in SCNF, respectively. The addition of ZIF-8 diminished the intensity of the characteristic SCNF peaks. The peak observed at 1,580 cm^{-1} was ascribed to the stretching vibration of C=N, and the peaks within the range of 1,460–1,300 cm^{-1} were related to the stretching of the 2-methylimidazole ring. The peak at 420 cm^{-1} was assigned to the Zn–N bond, indicative of the formation of a metal-ligand interaction [48]. The XRD and FTIR spectra further suggest that the ZIF-8 particles were effectively attached to the SCNF scaffold.

We also evaluated the *in situ* synthesis of SCNF with varying concentrations of ZIF-8 precursors to form different crystal sizes. As depicted in Fig. S4, hybrids from all three different loading concentrations of precursors retained the fibrous structure of SCNF, and the ZIF-8 particles adhered and distributed well along the SCNF surface. The size of the ZIF-8 crystals increased with increasing concentrations of the precursors. For example, at a lower concentration, *i.e.*, SCNF/ZIF-8 L, the size of ZIF-8 particles was around the tens of nanometers; with increased concentrations of zinc ions and 2-methylimidazole ligands, the crystal size grew to 100 nm for SCNF/ZIF-8 M; the highest concentration of precursors led to SCNF/ZIF-8 H with the crystalline size of approximately 400 nm. The three hybrids exhibited consistent XRD patterns and FTIR spectra (Fig. 4b and **c**), confirming the crystal and chemical structures were retained for both SCNF and ZIF-8. With increasing ZIF-8 loading concentrations to SCNF, a corresponding increase in signal intensity was observed, indicating a relatively higher proportion of ZIF-8 crystals in the hybrids. Prior study suggested that a higher precursor concentration can enhance the metal-ion diffusion rate, which then exceeds the termination kinetics of MOF nucleation. Consequently, this leads to the growth of larger MOF crystals [49]. TGA analysis revealed that the degradation of cellulose chains and the breakdown of glycosidic bonds in SCNF occurred at approximately 320 °C (Fig. S3b). However, the thermal decomposition of ZIF-8 was observed to occur at around 500 °C (Fig. S5). As the loading concentration of the ZIF-8 precursors increased, the SCNF/ZIF-8 hybrid showed improved thermal stability, and the weight of residue measured at 700 °C increased correspondingly. Owing to the significantly different thermal degradation temperatures between SCNF and ZIF-8, their respective mass ratios can be estimated from the TGA results at 700 °C [30]. The hybrids possessed a mass ratio of ZIF-8 of 47.0 %, 71.3 %, and 75.2 % for SCNF/ZIF8 L, SCNF/ZIF8 M, and SCNF/ZIF8 H, respectively. These results suggest that the size and the relative amount of ZIF-8 loaded onto the SCNF can be controlled by the concentration of the MOF precursors during the synthesis.

3.3. Robustness of SCNF as a scaffold for other MOFs

To demonstrate the versatility of SCNF as a biopolymer template for multiple MOFs, we performed the *in situ* synthesis of hybridizing SCNF with two other MOFs, *i.e.*, ZIF-67 and HKUST-1, representing different topology and functionalities of MOFs. The ZIF-67 content in the hybrids was determined to be 69.3 %, and the HKUST-1 content in the hybrids was 82.3 %. Similar to ZIF-8, ZIF-67 is another type of zeolitic imidazolate framework, with cobalt ions in a tetrahedral arrangement with the 2-methylimidazole ligand serving as an organic linker [50]. SEM imaging revealed ZIF-67 particles exhibiting rhombic dodecahedral shapes with diameters of around 800 nm (Fig. 5a). MOF HKUST-1 consists of copper ions linked by BTC ligands. The coordination between copper ions and BTC ligands forms paddlewheel-like primary units, which are connected by the organic linker to form a *tbo* topology [51]. The SEM images of HKUST-1 revealed octahedral or truncated octahedral particles with sizes of approximately 1 μm (Fig. 5b). Both ZIF-67 and HKUST-1 were successfully synthesized and hybridized on SCNF by *in situ* growth employing a similar synthesis approach for SCNF/ZIF-8. The cobalt ions in the ZIF-67 and the copper ions in the HKUST-1 initially interacted with the SCNF, likely at the $–SO_3^-$. As 2-methylimidazole or BTC ligands were introduced, the ZIF-67 and HKUST-1 crystals began to nucleate onto the SCNF [29]. The elemental

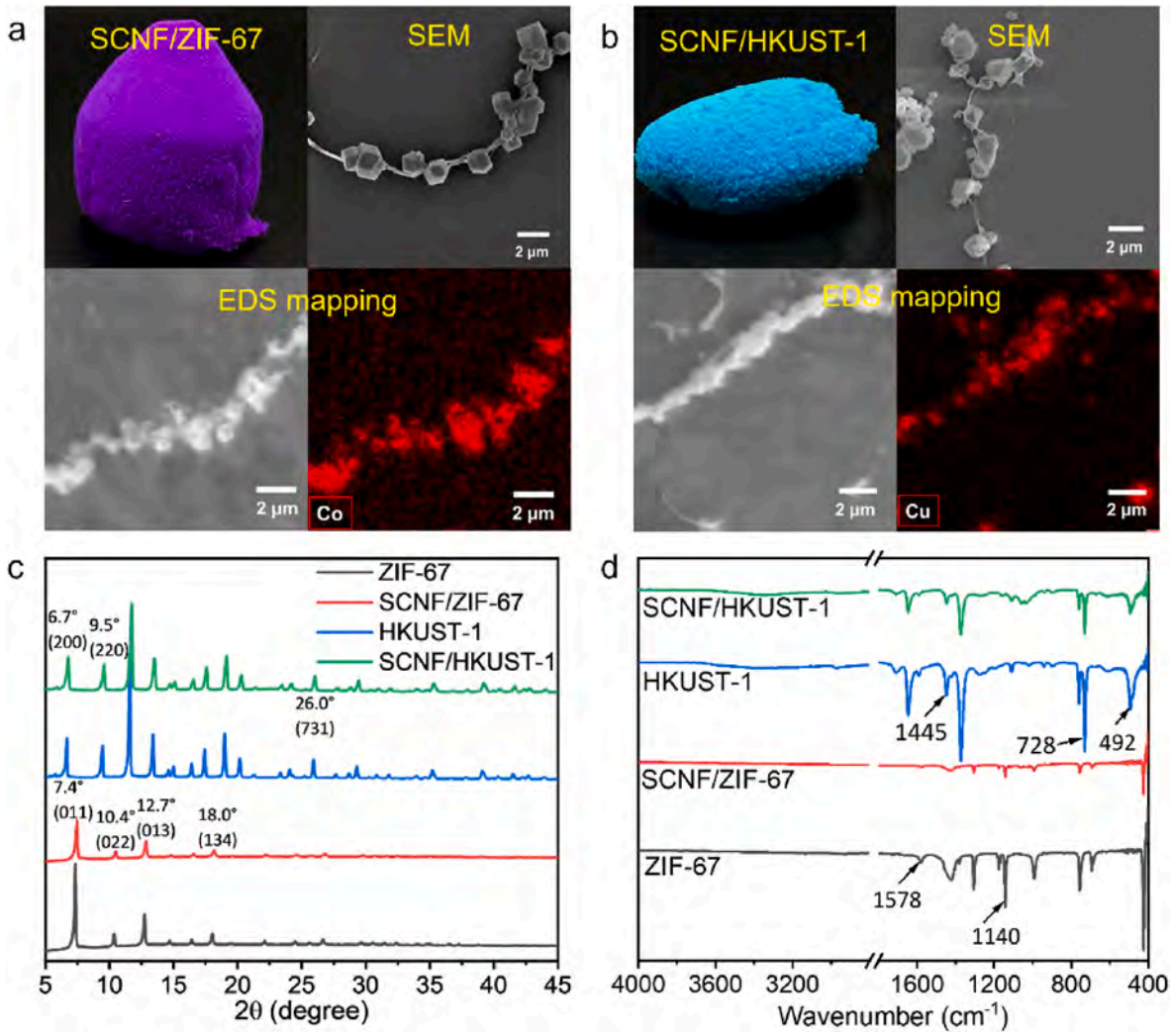

Fig. 5. Characterization of SCNF/ZIF-67 and SCNF/HKUST-1: visual appearance, SEM images, and EDS mappings of SCNF/ZIF-67 (a) and SCNF/HKUST-1 (b), XRD patterns (c), and FTIR spectra (d).

mapping results revealed that the copper and cobalt elements were evenly distributed along the SCNF (Fig. 5a and b), confirming that the ZIF-67 and HKUST-1 particles were anchored onto the SCNF surface.

The diffraction peaks at 2θ values of 7.4, 10.4, 12.7, and 18.0° of the XRD spectra corresponded to the characteristic planes (011), (022), (013), and (134) of the ZIF-67 crystals, respectively (Fig. 5c) [50]. Likewise, the diffraction peaks at 2θ of 6.7, 9.5, and 26.0° were associated with the characteristic planes (200), (220), and (731) of HKUST-1 crystals, respectively [52]. These XRD spectroscopic results further confirmed the presence of ZIF-67 and HKUST-1 crystals on the SCNF substrate. Moreover, the presence of SCNF did not alter the XRD patterns of the two MOFs, indicating that the characteristic lattice patterns of both ZIF-67 and HKUST-1 were preserved on the substrate. The FTIR spectra were analyzed to further characterize the structures of ZIF-67 and HKUST-1 (Fig. 5d). For ZIF-67, the peaks at 1,578 cm^{-1} and 1,140 cm^{-1} corresponded to the stretching vibrations of the C=N and C–N bonds in 2-methylimidazole, respectively. For HKUST-1, the peak at 1,445 cm^{-1} was attributed to the stretching vibration of the O=C–O group. The peaks at 728 cm^{-1} and 492 cm^{-1} were assigned to the stretching vibrations of the Cu–O bond.

MOFs are characterized by their porous crystalline framework, which gives them a high surface area [48]. We probed the specific surface areas of the pristine MOFs and their hybrids with the SCNF template to study the influence of hybridization. The BET specific surface areas of pristine ZIF-8, ZIF-67, and HKUST-1 particles were determined to be 1,564 m^2/g, 1,486 m^2/g, and 1,320 m^2/g, respectively (Table 1). Previous studies have also reported the high surface areas of these MOFs, exceeding 1,000 m^2/g, which is attributed to their highly porous nature [53]. After hybridization with SCNF, the three SCNF/MOFs showed substantially high surface areas, more than 1,000 m^2/g despite the hybrids having slightly lower surface area than their MOF counterparts (by ~ 200–300 m^2/g lower). This retention of surface area is largely attributed to the microporous MOF components in the hybrid material [54]. The high surface areas of the hybrids could potentially make them suitable for broad applications, including gas storage, catalysis, and selective adsorption [12].

Table 1
Surface areas of different MOFs and SCNF/MOF hybrids with the mass percentage of each MOF in the hybrid.

	ZIF-8	SCNF/ZIF-8 (75.2 wt %)	ZIF-67	SCNF/ZIF-67 (69.3 wt %)	HKUST-1	SCNF/HKUST-1 (82.3 wt%)
BET surface area (m^2/g)	1,564	1,237	1,486	1,119	1,320	1,120

3.4. Removal of methylene blue using SCNF/ZIF-8

Methylene blue is a widely used dye in various industries, and its presence in water poses potential risks to both environmental ecosystems and public health [55]. ZIF-8 was integrated with 2 % SCNF to form a free-standing aerogel. The effectiveness of the hybrid material was subsequently assessed for its ability to adsorb methylene blue in an aqueous environment. As shown in Fig. 6, both SCNF and SCNF/ZIF-8 aerogels achieved a remarkable removal efficiency ($C_e/C_0 < 20$ %) when the initial concentration of methylene blue was 20 mg/L or less. The pristine SCNF aerogel achieved a peak adsorption capacity of 22.3 mg/g for methylene blue. Notably, the SCNF aerogel showed pronounced effectiveness in adsorbing methylene blue at lower concentrations. This efficacy can be attributed to the negatively charged $-SO_3^-$ groups on SCNF, which exhibit a strong affinity for cationic compounds such as methylene blue [56]. Similarly, grafting $-SO_3^-$ groups onto chitosan has been observed to significantly boost its methylene blue adsorption capacity [57]. The incorporation of ZIF-8 into the SCNF aerogel led to a significant improvement in its adsorption capacity. The SCNF/ZIF-8 hybrid demonstrated a maximum adsorption efficiency of 62.04 mg/g, which is about 3 times that of the SCNF alone. The enhanced adsorption results from the porous architecture of ZIF-8 crystals, which provides a substantial surface area for interaction with methylene blue. Moreover, the ZIF-8 ligand has been reported to potentially attract methylene blue through electrostatic interactions [58].

We used the Langmuir and Freundlich models to interpret the adsorption behavior of the aerogels. The Langmuir model assumes the monolayer adsorption of solute onto a homogeneous adsorbent surface [59]. The model predicts that the adsorption process is reversible and that the adsorption sites are saturated at a certain concentration of solute, which can be expressed as:

$$\frac{C_e}{Q_e} = \frac{1}{Q_m K_L} + \frac{C_e}{Q_m}$$

where C_e (mg/L) is the equilibrium concentration of the methylene blue, Q_e (mg/g) is the equilibrium adsorption capacity of the adsorbent, Q_m (mg/g) is the maximum adsorption capacity of the adsorbent, and K_L is the Langmuir constant related to the energy of adsorption. The Freundlich model assumes a multilayer adsorption process on a heterogeneous surface and that the adsorption energy decreases as more solute is adsorbed [60]. The Freundlich model can be expressed as:

$$\ln Q_e = \ln K_F + \frac{1}{n} \ln C_e$$

where K_F is the Freundlich constant associated with the adsorption capacity, and n is the Freundlich exponent related to the adsorption intensity. The fitted isotherm model suggests that the Langmuir isotherm model fitted the adsorption data of SCNF better, as the R^2 value of the Langmuir isotherm model (0.998) was greater compared with that of the Freundlich isotherm model (0.839) (Fig. 6c and **d**). The adsorption data of the SCNF/ZIF-8 hybrid fitted well with both the Langmuir and Freundlich isotherm models. These results suggest that the adsorption of methylene blue on the SCNF adsorbent was a monolayer adsorption process with a homogeneous distribution of molecules on the adsorption sites. In contrast, the adsorption behavior of the SCNF/ZIF-8 hybrid appeared to occur on a heterogeneous surface or a mix of both monolayer and multilayer adsorption, with the adsorption capacity increasing as the concentration of methylene blue increases. The results can be explained by the structural difference between SCNF and ZIF-8: the monolayer adsorption of methylene blue to the SCNF is through electrostatic affinity that occurs due to the $-SO_3^-$ groups on the nanocellulose fibers, whereas the multilayer adsorption of methylene blue to the ZIF-8 occurs due to its porous structure. Previous studies have reported a maximum adsorption efficiency of 46.6 mg/g for methylene blue on ZIF-

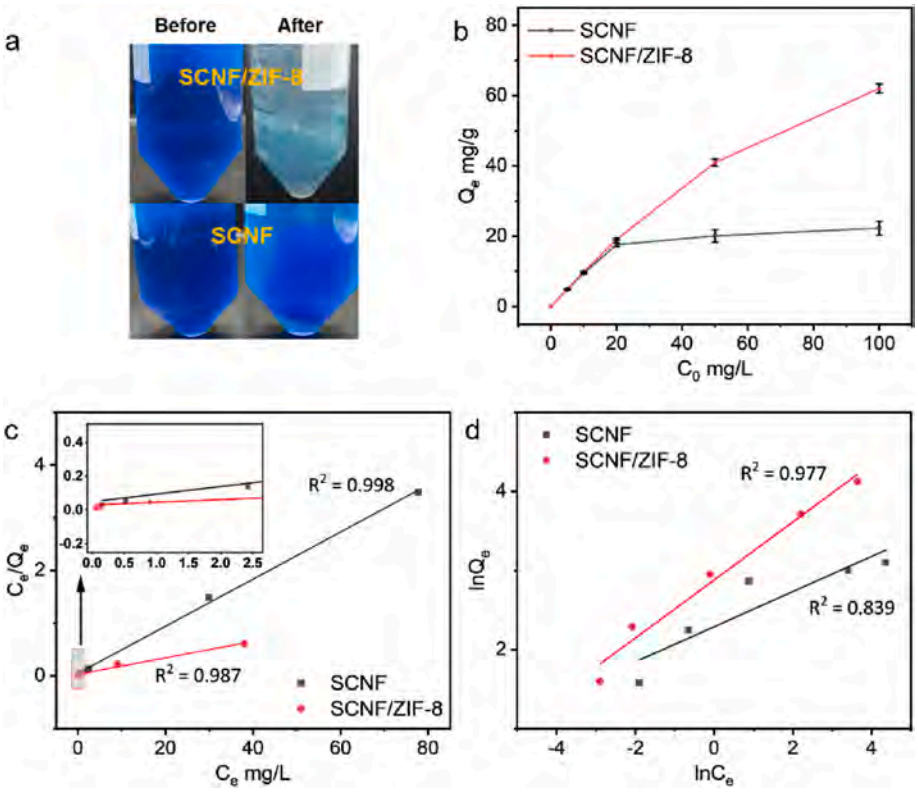

Fig. 6. Visual comparison before and after adsorption at 50 mg/L of methylene blue (a), adsorption capacities across different methylene blue concentrations per 20 mg sorbent (b), Langmuir fitting curves (c), and Freundlich fitting curves (d).

8, which was attributed to the diffusion and penetration of methylene blue into the ZIF-8 framework [61]. In another study, researchers synthesized a cellulose aerogel with ZIF-8 and observed the highest adsorption efficiency of 90.2 mg/g for methylene blue [54]. The results in our work were relatively lower than the previous study, and the difference in capacity might be due to variations in the loading capacity of ZIF-8. The SCNF/ZIF-8 hybrid in its current form lacks regenerability due to the long-term instability tendency of ZIF-8 and the limited mechanical strength of the SCNF aerogel, which can be addressed by using more stable MOFs and cross-linked SCNF. Additionally, it is important to highlight that the water stability of different MOFs varies significantly. Therefore, when designing SCNF-based adsorbents for use in aqueous or moisture-rich environments, careful consideration must be given to the potential decomposition of the selected MOFs.

DFT calculations were performed to rationalize the adsorption mechanism. To simplify the molecular structure, a SCNF model composed of a glucose monomer with sulfonic acid groups at C2 and C3 positions was selected to represent the SCNF structure, and a zinc atom with three 2-methylimidazole ligands was adopted to represent the ZIF-8 structure. For a complete full ZIF-8 periodic structure, zinc ions are tetrahedrally coordinated with four ligands and electrically neutral. On the surface, there may be one imidazole missing, potentially resulting in a net positive charge; however, the geometry around Zn^{2+} remains largely unchanged. Our simplified model, therefore, represents an imidazolate-terminated surface with potential hydrogen bonding sites [33,62,63]. The optimized geometries for SCNF, ZIF-8, and methylene blue clusters are illustrated in Fig. 7. The electrostatic potential surface mapping of SCNF predominantly revealed a red hue, indicating an overall negative charge. The charge was predominantly concentrated on the sulfonate groups, specifically on the S13-O14, O15, and O16 atoms. Natural Population Analysis (NPA) was employed to calculate the atomic charges. As depicted in Fig. 7, the resultant NPA charges were +2.429 for the S13 atom, −1.032 for the O14 atom, −1.066 for the O15 atom, and −1.069 for the O16 atom, suggesting them as potential bonding receptor sites [64]. For the ZIF-8 cluster, a notable yellow shade appeared on the outer nitrogen atom of the 2-methylimidazole ligand, specifically the N11 atom with an NPA charge of −0.550, identifying it as a potential binding site. Methylene blue, on the other hand, displayed a predominantly light blue hue, indicating an overall positive charge. This charge was particularly concentrated on the external methyl group, specifically the C3-H25 and C1-H23 atoms (and their counterparts). Therefore, the interaction between SCNF and methylene blue mainly occurred between SCNF's sulfonic acid groups and methylene blue's methyl group. The interaction between ZIF-8 and methylene blue was centered around the N atoms on the outer side of the ZIF-8 ligand and the terminal methyl groups of methylene blue.

The optimized SCNF and ZIF-8 clusters were combined with methylene blue to calculate the interaction energy between them. Consistent with the binding sites inferred from the electrostatic potential map, the optimized geometry results demonstrated that the sulfonate groups in SCNF interacted with the terminal methyl groups of methylene blue, while the nitrogen atoms on ZIF-8 ligands also engaged with these methyl ends (Fig. 7). Interaction strength correlates with bond length: longer bond lengths indicate weaker interactions [65]. The optimized geometry of the complex showed the bond lengths between the two O atoms on SCNF and the H atoms on methylene blue ranged between 2.23 Å and 2.45 Å. The bond lengths were around 2.40 Å between the N atoms on ZIF-8's ligand and the H atoms on methylene blue (Fig. 7), suggesting non-bonded interactions between both ZIF-8 and SCNF with methylene blue. The energy values for each optimized cluster are summarized in Table S2. DFT calculations showed that the binding energies for interactions with methylene blue were −5.80 eV for SCNF and −2.63 eV for ZIF-8. These negative values suggest that the adsorption was energetically favorable. These computational results indicate that both SCNF and ZIF-8 can spontaneously interact with methylene blue at a molecular level, with SCNF exhibiting a stronger binding energy than ZIF-8. However, given its high porosity and multilayer adsorption option, ZIF-8 offered an abundance of binding sites to engage with methylene blue, which played a crucial role in its adsorption performance.

4. Conclusion

In conclusion, this study explored the suitability of SCNF as a flexible biopolymer substrate for templating the synthesis of MOFs. The

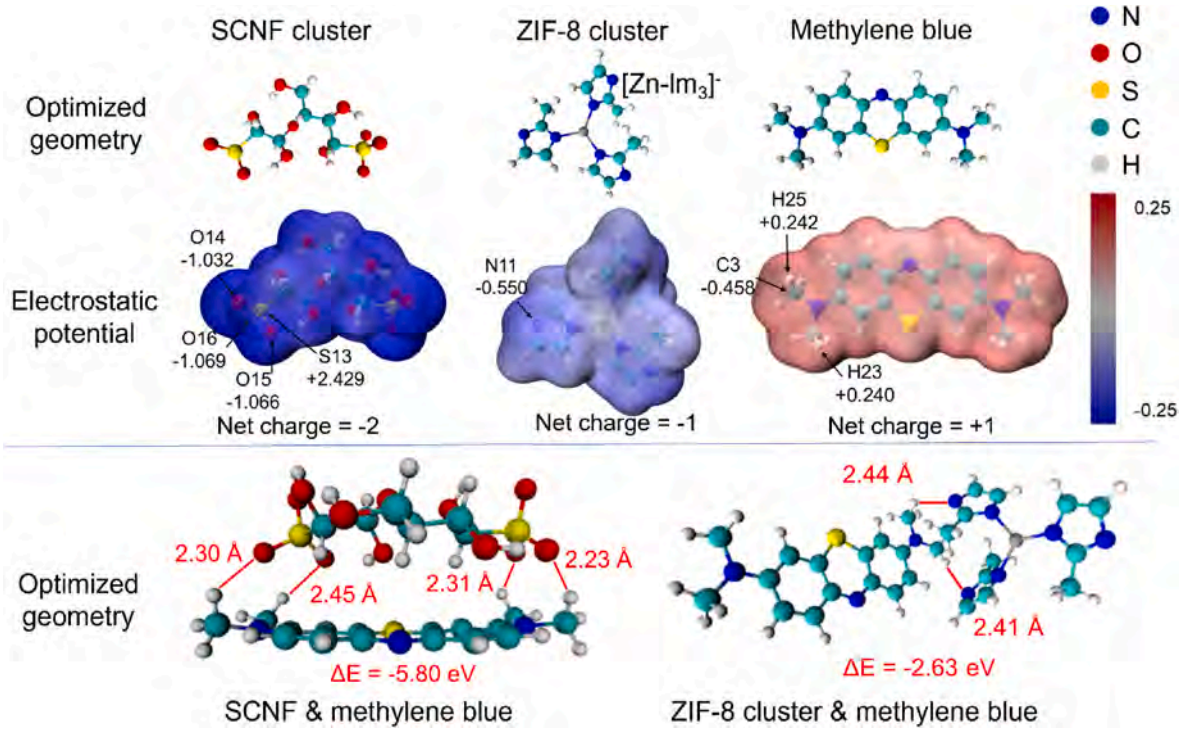

Fig. 7. Optimized geometries and electrostatic potential mappings of SCNF cluster, ZIF-8 cluster, and methylene blue, and optimized geometries of the complexes.

sulfonation of cellulose was achieved through the oxidation and bisulfite sulfonation reactions. The modification increased the fiber's dispersibility by introducing sulfonate groups. These functional groups bearing negative charges on the SCNF surface acted as potential binding sites for the nucleation of MOFs, revealed by the *in situ* synthesis of several MOFs, including ZIF-8, ZIF-67, and HKUST-1. This led to the formation of flexible SCNF/MOF hybrid materials with a distinctive fibrous necklace-like structure in which the MOFs were well-distributed along the fibrous cellulose. The SCNF substrate effectively reduced MOF agglomeration while retaining their high surface areas in the hybrids. Our results demonstrated that the loading capacity of MOFs on SCNF can be tuned by varying the concentrations of MOF precursors during the synthesis. We then evaluated the adsorptive capacity of the SCNF/ZIF-8 hybrid for methylene blue. The hybrid exhibited enhanced dye adsorption capacity compared with the SCNF control. Adsorption model analysis further suggests that the adsorption by the SCNF/ZIF-8 hybrid involved a multilayer process on a heterogeneous surface, attributed to the pronounced porosity of ZIF-8, whereas the adsorption with SCNF showed a monolayer process on the surface of the cellulosic fibers. DFT calculation revealed that both SCNF and ZIF-8 exhibit favorable interactions with methylene blue. The sulfonate groups within the SCNF and the nitrogen atoms in ZIF-8 ligands can engage in non-bonded interactions with the terminal methyl groups of methylene blue. The results validate our hypothesis that SCNF can serve as an effective and flexible templating substrate for the design and engineering of various MOF hybrids. The SCNF/ZIF-8 hybrid showed enhanced adsorption capacity for methylene blue, highlighting the hybrid's potential as robust adsorbents for the removal of organic dyes from aqueous solutions. However, the coordination mechanism of the MOFs nanoparticles with SCNF and $-SO^{3-}$ in particular, worths of unmasking in future studies.

CRediT authorship contribution statement

Kailong Zhang: Writing – original draft, Investigation, Formal analysis, Data curation, Conceptualization. **William Hutcherson:** Writing – review & editing, Investigation, Data curation. **Neal D. Evans:** Writing – review & editing, Formal analysis, Data curation. **Thomas Elder:** Writing – review & editing, Resources, Formal analysis. **Charles M. Garner:** Writing – review & editing, Methodology, Investigation, Formal analysis, Data curation. **Mi Li:** Writing – review & editing, Validation, Supervision, Resources, Project administration, Methodology, Investigation, Funding acquisition, Formal analysis, Data curation, Conceptualization.

Declaration of competing interest

The authors declare that they have no known competing financial interests or personal relationships that could have appeared to influence the work reported in this paper.

Acknowledgments

This work was supported by the University of Tennessee-University of Memphis Collaborative Research Network program; the South-Eastern Regional Sun Grant Center at the University of Tennessee; and the US EPA's P3 program SU84087101. Electron microscopy and X-ray diffraction instrument access are provided by the Institute for Advanced Materials & Manufacturing at the University of Tennessee, Knoxville. The computation for this work was performed on the University of Tennessee Infrastructure for Scientific Applications and Advanced Computing computational resources.

Appendix. ASupplementary data

Supplementary data to this article can be found online at https://doi.org/10.1016/j.solidstatesciences.2024.107755.

Data availability

Data will be made available on request.

References

[1] A.J. Howarth, Y. Liu, P. Li, Z. Li, T.C. Wang, J.T. Hupp, O.K. Farha, Chemical, thermal and mechanical stabilities of metal–organic frameworks, Nat. Rev. Mater. 1 (3) (2016) 1–15.
[2] H. Li, M. Eddaoudi, M. O'Keeffe, O.M. Yaghi, Design and synthesis of an exceptionally stable and highly porous metal-organic framework, Nature 402 (6759) (1999) 276–279.
[3] A. Corma, H. Garcia, F. Llabrés i Xamena, Engineering metal organic frameworks for heterogeneous catalysis, Chem. Rev. 110 (8) (2010) 4606–4655.
[4] H. Furukawa, K.E. Cordova, M. O'Keeffe, O.M. Yaghi, The chemistry and applications of metal-organic frameworks, Science 341 (6149) (2013) 1230444.
[5] L. Jiao, J.Y.R. Seow, W.S. Skinner, Z.U. Wang, H.-L. Jiang, Metal–organic frameworks: structures and functional applications, Mater. Today 27 (2019) 43–68.
[6] W.-T. Koo, J.-S. Jang, I.-D. Kim, Metal-organic frameworks for chemiresistive sensors, Chem 5 (8) (2019) 1938–1963.
[7] X. Zhao, Y. Wang, D.S. Li, X. Bu, P. Feng, Metal–organic frameworks for separation, Adv. Mater. 30 (37) (2018) 1705189.
[8] Y.S. Li, H. Bux, A. Feldhoff, G.L. Li, W.S. Yang, J. Caro, Controllable synthesis of metal–organic frameworks: from MOF nanorods to oriented MOF membranes, Adv. Mater. 22 (30) (2010) 3322–3326.
[9] J.-Q. Shen, P.-Q. Liao, D.-D. Zhou, C.-T. He, J.-X. Wu, W.-X. Zhang, X.-M. Chen, Modular and stepwise synthesis of a hybrid metal–organic framework for efficient electrocatalytic oxygen evolution, J. Am. Chem. Soc. 139 (5) (2017) 1778–1781.
[10] P. Falcaro, R. Ricco, C.M. Doherty, K. Liang, A.J. Hill, M.J. Styles, MOF positioning technology and device fabrication, Chem. Soc. Rev. 43 (16) (2014) 5513–5560.
[11] A. Isogai, T. Saito, H. Fukuzumi, TEMPO-oxidized cellulose nanofibers, Nanoscale 3 (1) (2011) 71–85.
[12] H.N. Abdelhamid, A.P. Mathew, Cellulose–metal organic frameworks (CelloMOFs) hybrid materials and their multifaceted Applications: a review, Coord. Chem. Rev. 451 (2022) 214263.
[13] M. da Silva Pinto, C.A. Sierra-Avila, J.P. Hinestroza, In situ synthesis of a Cu-BTC metal–organic framework (MOF 199) onto cellulosic fibrous substrates: cotton, Cellulose 19 (2012) 1771–1779.
[14] E. Laurila, J. Thunberg, S.P. Argent, N.R. Champness, S. Zacharias, G. Westman, L. Öhrström, Enhanced synthesis of metal-organic frameworks on the surface of electrospun cellulose nanofibers, Adv. Eng. Mater. 17 (9) (2015) 1282–1286.
[15] J. Thunberg, S.C. Zacharias, M. Hasani, O.A. Oyetunji, F.M.A. Noa, G. Westman, L. Öhrström, Hybrid metal-organic framework-cellulose materials retaining high porosity: ZIF-8@ cellulose nanofibrils, Inorganics 9 (11) (2021) 84.
[16] K. Zhang, T. Elder, Z. Cheng, K. Zhan, Y. Peng, M. Li, Cellulose nanofiber-templated metal-organic frameworks for fluorescent detection of methyl parathion pesticides, J. Environ. Chem. Eng. 12 (3) (2024) 112670.
[17] H. Fukuzumi, R. Tanaka, T. Saito, A. Isogai, Dispersion stability and aggregation behavior of TEMPO-oxidized cellulose nanofibrils in water as a function of salt addition, Cellulose 21 (2014) 1553–1559.
[18] J. Luo, N. Semenikhin, H. Chang, R.J. Moon, S. Kumar, Post-sulfonation of cellulose nanofibrils with a one-step reaction to improve dispersibility, Carbohydr. Polym. 181 (2018) 247–255.
[19] J. Zhang, N. Jiang, Z. Dang, T.J. Elder, A.J. Ragauskas, Oxidation and sulfonation of cellulosics, Cellulose 15 (2008) 489–496.
[20] F. Sun, W. Liu, Z. Dong, Y. Deng, Underwater superoleophobicity cellulose nanofibril aerogel through regioselective sulfonation for oil/water separation, Chem. Eng. J. 330 (2017) 774–782.
[21] A.P. Côté, G.K. Shimizu, The supramolecular chemistry of the sulfonate group in extended solids, Coord. Chem. Rev. 245 (1–2) (2003) 49–64.
[22] Y. Wang, Y. Wang, C. Chen, X. Chen, Q. Zhao, L. Yang, Z. Jiang, Optimizing the sulfonic groups of a polymer to coat the zinc anode for dendrite suppression, Chem. Commun. 57 (43) (2021) 5326–5329.
[23] S.K. Mäkinen, N.J. Melcer, M. Parvez, G.K. Shimizu, Highly selective guest uptake in a silver sulfonate network imparted by a tetragonal to triclinic shift in the solid state, Chem.–Eur. J. 7 (23) (2001) 5176–5182.
[24] S. Lander, J. Erlandsson, M. Vagin, V. Gueskine, L. Korhonen, M. Berggren, X. Crispin, Sulfonated cellulose membranes: physicochemical properties and ionic transport versus degree of sulfonation, Adv. Sustain. Syst. 6 (11) (2022) 2200275.
[25] P.A. Larsson, M. Gimåker, L. Wågberg, The influence of periodate oxidation on the moisture sorptivity and dimensional stability of paper, Cellulose 15 (2008) 837–847.
[26] H. Zhao, N.D. Heindel, Determination of degree of substitution of formyl groups in polyaldehyde dextran by the hydroxylamine hydrochloride method, Pharmaceut. Res. 8 (1991) 400–402.
[27] D. Rajalaxmi, N. Jiang, G. Leslie, A.J. Ragauskas, Synthesis of novel water-soluble sulfonated cellulose, Carbohydr. Res. 345 (2) (2010) 284–290.
[28] L. Fliri, K. Heise, T. Koso, A.R. Todorov, D.R. Del Cerro, S. Hietala, A.W. King, Solution-state nuclear magnetic resonance spectroscopy of crystalline cellulosic materials using a direct dissolution ionic liquid electrolyte, Nat. Protoc. 18 (7) (2023) 2084–2123.

[29] S.C. Li, B.C. Hu, L.M. Shang, T. Ma, C. Li, H.W. Liang, S.H. Yu, General synthesis and solution processing of metal–organic framework nanofibers, Adv. Mater. 34 (29) (2022) 2202504.
[30] L. Zhu, L. Zong, X. Wu, M. Li, H. Wang, J. You, C. Li, Shapeable fibrous aerogels of metal–organic-frameworks templated with nanocellulose for rapid and large-capacity adsorption, ACS Nano 12 (5) (2018) 4462–4468.
[31] A.D. French, Idealized powder diffraction patterns for cellulose polymorphs, Cellulose 21 (2) (2014) 885–896.
[32] L. Segal, J.J. Creely, A. Martin Jr, C. Conrad, An empirical method for estimating the degree of crystallinity of native cellulose using the X-ray diffractometer, Textil. Res. J. 29 (10) (1959) 786–794.
[33] C. Chizallet, S. Lazare, D. Bazer-Bachi, F. Bonnier, V. Lecocq, E. Soyer, N. Bats, Catalysis of transesterification by a nonfunctionalized metal− organic framework: acido-basicity at the external surface of ZIF-8 probed by FTIR and ab initio calculations, J. Am. Chem. Soc. 132 (35) (2010) 12365–12377.
[34] W. Hehre, R. Ditchfield, R. Stewart, J. Pople, self-consistent molecular orbital methods. iv. use of Gaussian expansions of Slater-type orbitals. Extension to second-row molecules, J. Chem. Phys. 52 (5) (1970) 2769–2773.
[35] S.F. Boys, F. Bernardi, The calculation of small molecular interactions by the differences of separate total energies. Some procedures with reduced errors, Mol. Phys. 19 (4) (1970) 553–566.
[36] T. Lu, F. Chen, Multiwfn: a multifunctional wavefunction analyzer, J. Comput. Chem. 33 (5) (2012) 580–592.
[37] U.-J. Kim, S. Kuga, M. Wada, T. Okano, T. Kondo, Periodate oxidation of crystalline cellulose, Biomacromolecules 1 (3) (2000) 488–492.
[38] H. Amer, T. Nypelö, I. Sulaeva, M. Bacher, U. Henniges, A. Potthast, T. Rosenau, Synthesis and characterization of periodate-oxidized polysaccharides: dialdehyde xylan (DAX), Biomacromolecules 17 (9) (2016) 2972–2980.
[39] J.P. Misiewicz, K.B. Moore III, P.R. Franke, W.J. Morgan, J.M. Turney, G. E. Douberly, I.I.I.H.F. Schaefer, Sulfurous and sulfonic acids: predicting the infrared spectrum and setting the surface straight, J. Chem. Phys. 152 (2) (2020) 024302.
[40] Y. Zhang, C. Wang, Y. Liu, W. Jiang, G. Han, Preparation and characterization of composite scaffold of alginate and cellulose nanofiber from ramie, Textil. Res. J. 89 (16) (2019) 3260–3268.
[41] R. Kheam, K. Zhang, T. Elder, N. Bryant, A. Ragauskas, M.I. Li, Totally chlorine-free peracetic acid pulping for nanocellulose isolation from hemp and poplar, TAPPI J. 22 (8) (2023) 529–540.
[42] F. D'Acierno, W.Y. Hamad, C.A. Michal, M.J. MacLachlan, Thermal degradation of cellulose filaments and nanocrystals, Biomacromolecules 21 (8) (2020) 3374–3386.
[43] C. Dong, F. Zhang, Z. Pang, G. Yang, Efficient and selective adsorption of multi-metal ions using sulfonated cellulose as adsorbent, Carbohydr. Polym. 151 (2016) 230–236.
[44] T. Bayer, B.V. Cunning, B. Šmíd, R. Selyanchyn, S. Fujikawa, K. Sasaki, S.M. Lyth, Spray deposition of sulfonated cellulose nanofibers as electrolyte membranes in fuel cells, Cellulose 28 (2021) 1355–1367.
[45] R.J. Moon, A. Martini, J. Nairn, J. Simonsen, J. Youngblood, Cellulose nanomaterials review: structure, properties and nanocomposites, Chem. Soc. Rev. 40 (7) (2011) 3941–3994.
[46] S. Fujisawa, K. Daicho, A. Yurtsever, T. Fukuma, T. Saito, Molecular dynamics of drying-induced structural transformations in a single nanocellulose, Small (2023) 2302276.
[47] Y.-R. Lee, M.-S. Jang, H.-Y. Cho, H.-J. Kwon, S. Kim, W.-S. Ahn, ZIF-8: a comparison of synthesis methods, Chem. Eng. J. 271 (2015) 276–280.
[48] K. Cho, L.J. Andrew, M. MacLachlan, Uniform growth of nanocrystalline ZIF-8 on cellulose nanocrystals: useful template for microporous organic polymers, Angew. Chem. Int. Ed. (2023) e202300960.
[49] C.R. Marshall, S.A. Staudhammer, C.K. Brozek, Size control over metal–organic framework porous nanocrystals, Chem. Sci. 10 (41) (2019) 9396–9408.
[50] G. Zhong, D. Liu, J. Zhang, The application of ZIF-67 and its derivatives: adsorption, separation, electrochemistry and catalysts, J. Mater. Chem. A 6 (5) (2018) 1887–1899.
[51] C.H. Hendon, A. Walsh, Chemical principles underpinning the performance of the metal–organic framework HKUST-1, Chem. Sci. 6 (7) (2015) 3674–3683.
[52] Z. Chen, X. He, J. Ge, G. Fan, L. Zhang, A.M. Parvez, G. Wang, Controllable fabrication of nanofibrillated cellulose supported HKUST-1 hierarchically porous membranes for highly efficient removal of formaldehyde in air, Ind. Crop. Prod. 186 (2022) 115269.
[53] E. Tsalaporta, J.D. MacElroy, A comparative study of the physical and chemical properties of pelletized HKUST-1, ZIF-8, ZIF-67 and UiO-66 powders, Heliyon 6 (9) (2020) e04883.
[54] G. Wu, C. Zhou, H. Li, S. Xia, Y. Zhu, J. Han, W. Xing, Controlled fabrication of the biomass cellulose aerogel@ ZIF-8 nanocomposite as efficient and recyclable adsorbents for methylene blue removal, Ind. Crop. Prod. 193 (2023) 116169.
[55] E. Santoso, R. Ediati, Y. Kusumawati, H. Bahruji, D. Sulistiono, D. Prasetyoko, Review on recent advances of carbon based adsorbent for methylene blue removal from waste water, Mater. Today Chem. 16 (2020) 100233.
[56] N.S. El-Sayed, A. Salama, V. Guarino, Coupling of 3-aminopropyl sulfonic acid to cellulose nanofibers for efficient removal of cationic dyes, Materials 15 (19) (2022) 6964.
[57] H. Shi, C. Dong, Y. Yang, Y. Han, F. Wang, C. Wang, J. Men, Preparation of sulfonate chitosan microspheres and study on its adsorption properties for methylene blue, Int. J. Biol. Macromol. 163 (2020) 2334–2345.
[58] E. Santoso, R. Ediati, Z. Istiqomah, D.O. Sulistiono, R.E. Nugraha, Y. Kusumawati, D. Prasetyoko, Facile synthesis of ZIF-8 nanoparticles using polar acetic acid solvent for enhanced adsorption of methylene blue, Microporous Mesoporous Mater. 310 (2021) 110620.
[59] I. Langmuir, The adsorption of gases on plane surfaces of glass, mica and platinum, J. Am. Chem. Soc. 40 (9) (1918) 1361–1403.
[60] H. Freundlich, Over the adsorption in solution, Z. Phys. Chem. 57 (1906) 358–471.
[61] B.L. Tran, H.-Y. Chin, B.K. Chang, A.S. Chiang, Dye adsorption in ZIF-8: the importance of external surface area, Microporous Mesoporous Mater. 277 (2019) 149–153.
[62] C. Chizallet, N. Bats, External surface of zeolite imidazolate frameworks viewed ab initio: multifunctionality at the organic− inorganic interface, J. Phys. Chem. Lett. 1 (1) (2010) 349–353.
[63] H. Wang, L. Zhao, W. Xu, S. Wang, Q. Ding, X. Lu, W. Guo, The properties of the bonding between CO and ZIF-8 structures: a density functional theory study, Theor. Chem. Acc. 134 (2015) 1–9.
[64] P. Zhou, X. Li, J. Zhou, Z. Peng, L. Shen, W. Li, Insights of the adsorption mechanism of methylene blue on biochar from phytoextraction residues of Citrus aurantium L.: adsorption model and DFT calculations, J. Environ. Chem. Eng. 11 (5) (2023) 110496.
[65] A. Lobato, M.A. Salvadó, J.M. Recio, M. Taravillo, V.G. Baonza, Highs and lows of bond lengths: is there any limit? Angew. Chem. 133 (31) (2021) 17165–17173.